

## Article

# Constructing Stable $\text{MoO}_x\text{-NiS}_x$ Film via Electrodeposition and Hydrothermal Method for Water Splitting

Shihu Zhu <sup>1,2</sup>, Tiantian Liu <sup>1,3</sup>, Shuang Yu <sup>1,3</sup>, Huijing Yang <sup>1,3</sup>, Qimeng Sun <sup>1,3</sup> and Jin You Zheng <sup>1,3,\*</sup> 

<sup>1</sup> Engineering Research Center of Advanced Functional Material Manufacturing of Ministry of Education, School of Chemical Engineering, Zhengzhou University, Zhengzhou 450001, China; 15638216421@163.com (S.Z.); ltt13429817116@163.com (T.L.); shuangyu\_225@163.com (S.Y.); huiging@163.com (H.Y.); qimeng\_sun1@163.com (Q.S.)

<sup>2</sup> School of Mechanical and Power Engineering, Zhengzhou University, Zhengzhou 450001, China

<sup>3</sup> National Key Laboratory of Coking Coal Green Process Research, Zhengzhou University, Zhengzhou 450001, China

\* Correspondence: jinyouzh@zzu.edu.cn

**Abstract:** The hydrothermal method is a frequently used approach for synthesizing HER electrocatalysts. However, a weak tolerance to high temperature is an intrinsic property of carbon cloth (CC) in most situations, and CC-based catalysts, which require complex technological processes in low-temperature environments, exhibit weak stability and electrochemical performance. Hence, we provide a new solution for these issues. In this work,  $\text{MoO}_3\text{-NiS}_x$  films of 9H5E-CC catalysts are synthesized, first through electrodeposition to form Ni particles on CC and then through a hydrothermal reaction to reform the reaction. The advantages of this synthetic process include mild reaction conditions and convenient operation. The obtained  $\text{MoO}_3\text{-NiS}_x$  film presents excellent catalytic activity and stability for HER.  $\text{MoO}_3\text{-NiS}_x$  film requires only a low overpotential of 142 mV to drive  $10 \text{ mA cm}^{-2}$  for HER in 1.0 m KOH, and the obtained 9H5E-CF film only needs 294 mV to achieve  $50 \text{ mA cm}^{-2}$  for OER. Remarkably, they also show excellent OER, HER, and full water splitting long-term electrochemical stability, maintaining their performance for at least 72 h. This work can be expanded to provide a new strategy for the fabrication of stable, high-performing electrodes using simple, mild reaction conditions.



**Citation:** Zhu, S.; Liu, T.; Yu, S.; Yang, H.; Sun, Q.; Zheng, J.Y. Constructing Stable  $\text{MoO}_x\text{-NiS}_x$  Film via Electrodeposition and Hydrothermal Method for Water Splitting. *Catalysts* **2023**, *13*, 1426. <https://doi.org/10.3390/catal13111426>

Academic Editor: Bruno Fabre

Received: 15 October 2023

Revised: 27 October 2023

Accepted: 30 October 2023

Published: 9 November 2023



**Copyright:** © 2023 by the authors. Licensee MDPI, Basel, Switzerland. This article is an open access article distributed under the terms and conditions of the Creative Commons Attribution (CC BY) license (<https://creativecommons.org/licenses/by/4.0/>).

**Keywords:** hydrothermal reaction;  $\text{MoO}_3\text{-NiS}_x$  film; electrodeposition and reforming reaction; anodizing

## 1. Introduction

Environmental pollution and the depletion of traditional energy sources have drawn widespread attention [1–4]. Alternative energy conversion and utilization are promising methods to solve these problems [5–8]. The hydrogen evolution reaction (HER) via water electrolysis is a potential candidate due to its eco-friendliness, high energy density, and sustainable utilization [9]. Nevertheless, the low current density and high energy barrier are the key factors limiting the water splitting efficiency of the HER [10,11]. Although platinum-based catalysts have a high current density with a low energy barrier, their scarcity and high price limit their large-scale utilization [12]. Therefore, exploiting Earth-abundant and low-cost nonprecious HER electrocatalysts is still challenging.

There has been a significant advancement in carbon cloth (CC)-template-based electrocatalysts, which have been proven to have a high specific surface area and electrical conductivity for the HER [13–16]. For the past few years, efforts have been made to develop synthetic technology and modify materials [17–22], such as hydrothermal synthesis, calcine, solvothermal strategy, and phosphorization, in order to use CC-based HER catalysts that have low overpotential and long-term durability [23–27]. Using a hydrothermal reaction and nitridation method, Yao et al. synthesized Cr-doped  $\text{Co}_4\text{N}$  nanorod arrays on CC ( $\text{Cr-Co}_4\text{N/CC}$ ), which had high efficiency for the HER in alkaline media [28]. Gu et al.

constructed a bifunctional electrocatalyst through the in situ growth of NiS/MoS<sub>2</sub> hetero-nanoflowers on a CC substrate [27]. Chen et al. fabricated a metal–organic framework hybrid nanostructure consisting of multiple transition metal phosphide (NiCoZnP) nanoclusters and hierarchical ultrathin N-doped carbon (NC) nanosheets for overall water splitting [29]. However, most CC-template-based electrocatalysts can only be used at low current densities. A -template-based catalysts often have a poor tolerance to high temperatures, necessitating the adoption of sophisticated technological techniques when the temperature is low. Some methods are too costly and time-consuming to be applied on a large scale. Therefore, it is highly desirable to fabricate low-cost electrocatalysts that perform well at low temperatures.

In this work, a MoO<sub>3</sub>-NiS<sub>x</sub> composite electrocatalyst was directly synthesized on a CC template (9H5E-CC) via electrodeposition and hydrothermal methods. 9H5E-CC exhibits excellent HER performance with long-term stability. Using a similar approach, a MoO<sub>3</sub>-NiS<sub>x</sub> composite OER electrocatalyst on a Co foam (9H5E-CF) was also synthesized by replacing CC with Co foam. The reconstitution of the hydrothermal reaction made the particles smaller than in the last step; this phenomenon was confirmed using scanning electron microscopy (SEM). X-ray diffraction (XRD) and X-ray photoelectron spectroscopy (XPS) also revealed the ingredients of the synthesized product of reconstitution. Likewise, electrochemical measurement further evidenced the strengthened performance after reconstitution. The product presented low overpotentials of 142 mV at 10 mA cm<sup>-2</sup> for HER and 294 mV at 50 mA cm<sup>-2</sup> for OER. 9H5E-CC was more stable than most other materials reported from hydrothermal synthesis.

## 2. Results and Discussion

A Ni particle film (5E-CC sample) was synthesized on CC via electrodeposition. For the electrodeposition solution, Na<sub>2</sub>SO<sub>4</sub> was used for the supporting electrolyte, which can improve the conductivity of a solution. NiSO<sub>4</sub> was utilized as a suitable Ni source. H<sub>3</sub>BO<sub>3</sub> can change the pH of an electrodeposition solution and control the electrodeposited layer's morphology. Then, a MoO<sub>3</sub>-NiS<sub>x</sub> film (9H5E-CC) was fabricated using the obtained 5E-CC sample for the hydrothermal reaction, as shown in Figure 1a and Table S1. While the hydrothermal processes primarily employed (NH<sub>4</sub>)<sub>2</sub>MoS<sub>4</sub> as a Mo source, CH<sub>4</sub>N<sub>2</sub>S generated sufficient S<sup>2-</sup> for the sulfuration reaction during the hydrothermal reaction. The first stage in the hydrothermal reaction is a redox reaction, which causes the electrodeposited Ni layer to dissolve as Ni<sup>2+</sup>/Ni<sup>3+</sup> ions, and then the Ni<sup>2+</sup>/Ni<sup>3+</sup> ions diffuse into a mixed solution with the increase in temperature. The next reaction step is the formation of a MoO<sub>3</sub>-NiS<sub>x</sub> catalyst film during the constant-temperature phase. The morphologies of the 5E-CC and 9H5E-CC samples are shown in Figure 2a,b. Figure 2a displays Ni particles with irregular shapes formed on carbon fibers after electrodeposition. The Ni particles stacked together to form a smooth and compact Ni-coating film. The average size of particles in the electrodeposited Ni layer was about 0.71 μm. After the hydrothermal reaction, large Ni particles converted into smaller and more compact MoO<sub>3</sub>-NiS<sub>x</sub> particles with average sizes of ca. 0.15 μm via the dissolution of Ni particles and re-reaction, as shown in Figure 2b. To prove that, the powder product was collected from the hydrothermal reaction for 30 min. Its composition was checked using SEM-EDS, as shown in Figure S1. The result reveals that the deposits contained the Ni element, confirming that the dissolution of Ni particles and re-reaction had occurred. Smaller particles help to provide abundant exposing surfaces and highly exposed active sites. Figure 2c reveals the morphology of the 9H5E-CC sample after long-term testing, whose morphology and structure almost remained constant for a long period of about 72 h while running under invariable current densities of 10, 20, and 100 mA cm<sup>-2</sup>, demonstrating excellent stability in HER processes. Furthermore, compared with the catalyst before long-term testing, the average grain diameter of the catalyst after long-term testing increased from 0.15 μm to 0.17 μm, an increase of only around 13%, proving the catalyst's remarkable stability.

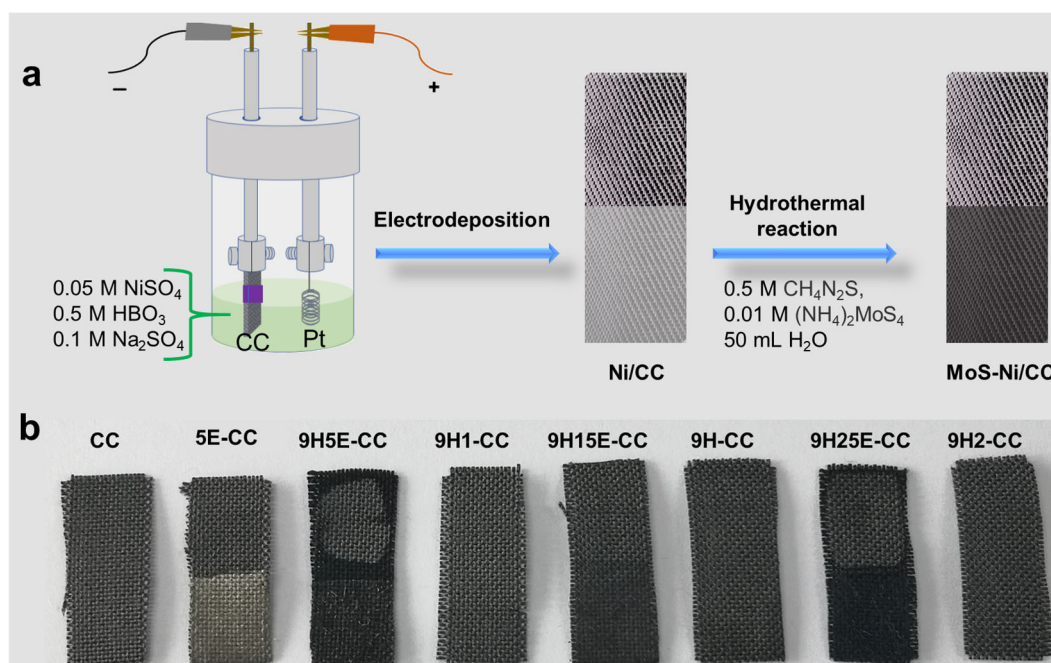


**Figure 1.** (a) Schematic illustration of the procedure for fabrication of MoO<sub>3</sub>-NiS<sub>x</sub> (9H5E-CC) electrode. (b) Photographic images of the CC substrate and the as-prepared samples.

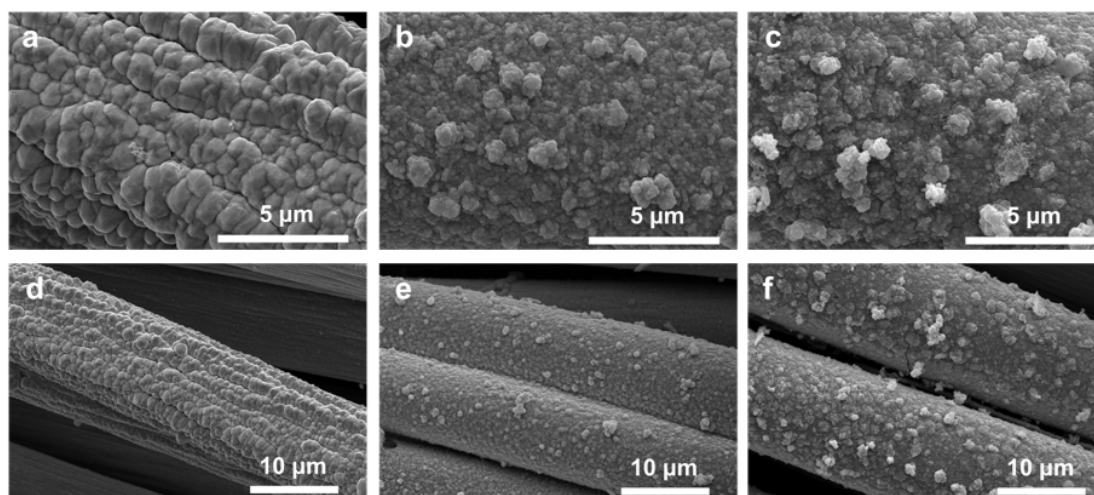


**Figure 2.** SEM images of (a,d) 5E-CC, (b,e) 9H5E-CC, and (c,f) 9H5E-CC after running chronopotentiometry.

The surface composition of the catalyst has a crucial effect on electrocatalytic activity. Various measurements were utilized to determine the surface composition of the samples. The XRD pattern of 5E-CC is shown in Figure S2, where every diffraction peak can be indexed to Ni (JCPDS: 04-0850). The pattern demonstrates that a metal Ni layer was coated on the CC substrate after electrodeposition. The XRD pattern of 9H5E-CC is shown in Figure 3a, where each diffraction peak can be indexed to MoO<sub>3</sub> (JCPDS: 21-0569), NiS<sub>2</sub> (JCPDS: 04-8683), and NiS (JCPDS: 06-6018). The combined distinctive peaks of MoO<sub>3</sub>, NiS<sub>2</sub>, and NiS are visible in 9H5E-CC, indicating the formation of a composite film after the hydrothermal reaction. The weak peaks of 9H5E-CC are attributed to the low crystallinity, which may have better electrochemical stability.

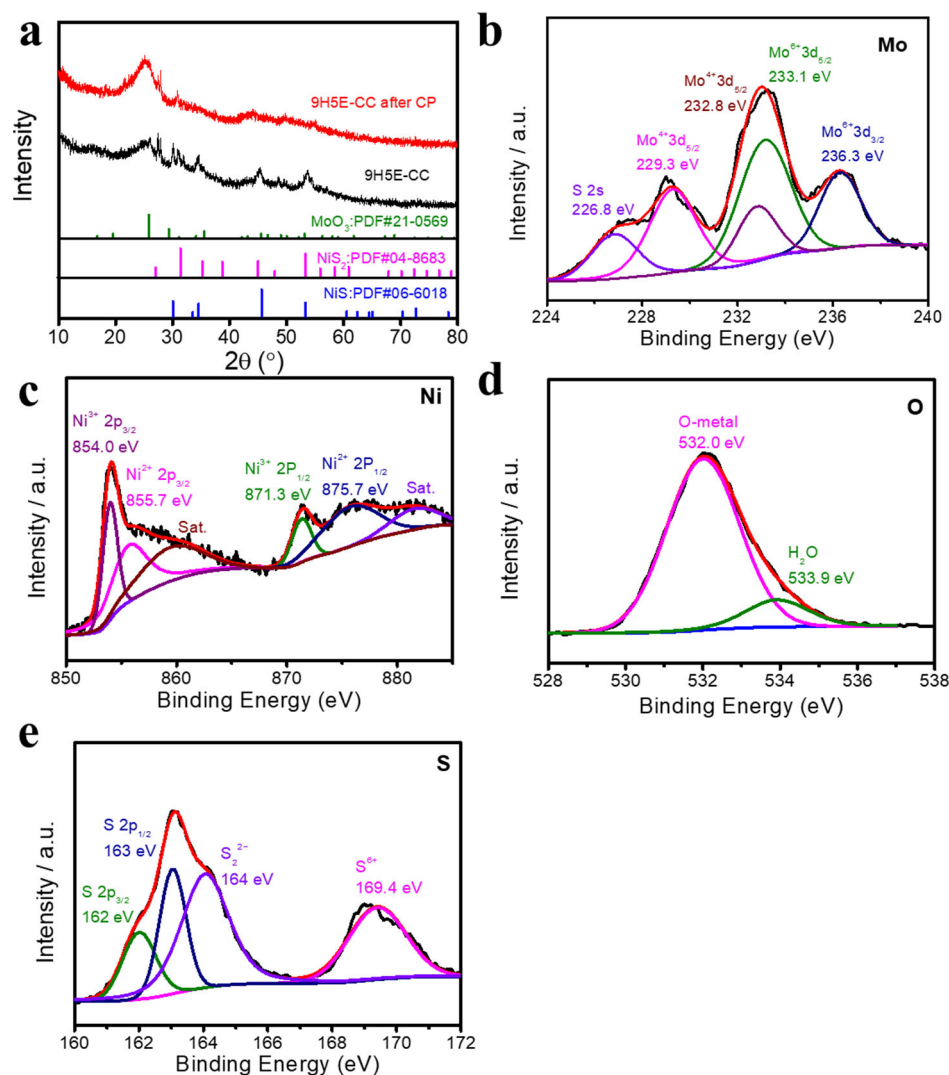


**Figure 3.** The oxidation states and chemical composition of 9H5E-CC: (a) XRD patterns. XPS analysis of (b) Mo, (c) Ni, (d) O, and (e) S.

The electrocatalytic activity is also significantly influenced by the chemical valence state. Mo, Ni, S, and O were present in 9H5E-CC according to the XPS analysis. The C1s peak at 284.8 eV was utilized as the standard peak throughout the XPS calibration procedure. The Mo 3d and S 2s XPS spectra for the 9H5E-CC are displayed in Figure 3b. The peaks at 229.3 eV and 232.8 eV are associated with the 3d<sub>5/2</sub> and 3d<sub>3/2</sub> of Mo<sup>4+</sup> for MoO<sub>3</sub>, respectively [30,31]. The peaks located at 233.1 eV and 236.3 eV are also attributed to Mo<sup>6+</sup> for MoO<sub>3</sub>. As shown in Figure 3c, the two strong Ni 2p peaks at 854.0 eV and 855.7 eV belong to Ni 2p<sub>3/2</sub>, and the peaks at 871.3 eV and 875.7 eV correspond to Ni 2p<sub>1/2</sub>, together with two satellite peaks at 859.41 eV and 881.54 eV. The small satellite peak around 226.8 eV is ascribed to S 2s for NiS<sub>2</sub> and NiS [32,33]. The peaks around 532.0 eV and 533.9 eV belong to surface-adsorbed H<sub>2</sub>O and O-Mo, as shown in Figure 3d [34]. The peaks located at 162.0 eV and 163.0 eV belong to S 2p<sub>3/2</sub> and S 2p<sub>1/2</sub>, as shown in Figure 3e. The peaks at 164.0 eV and 169.4 eV are related to S<sub>2</sub><sup>2-</sup> and S<sup>6+</sup>, respectively [35]. Based on XRD and XPS analysis, the as-synthesized 9H5E-CC catalyst was mainly composed of MoO<sub>3</sub>, NiS<sub>2</sub>, and NiS.

To further demonstrate the microstructure of the MoO<sub>3</sub>-NiS<sub>x</sub> electrocatalyst, the TEM results are displayed in Figure 4. Figure 4b,c show that the different lattice fringes of 0.253 nm, 0.199 nm, and 0.529 nm can be indexed to the NiS<sub>2</sub> (210), NiS (102), and MoO<sub>3</sub> (110) facets, respectively, in the HR-TEM images. The ring diffraction pattern

of SAED reveals that the  $\text{MoO}_3$ ,  $\text{NiS}_2$ , and  $\text{NiS}$  particles were polycrystalline structures, as shown in Figure 4d. The elemental mappings of Mo, Ni, S, and O are displayed in Figure 4e,f, which certify the uniform distribution of  $\text{MoO}_3$ ,  $\text{NiS}_2$ , and  $\text{NiS}$  particles on the surface of the 9H5E-CC sample. The distribution of element concentration of Mo and Ni corresponds to O and S, which proves the main contents existed in the form of  $\text{MoO}_3$ ,  $\text{NiS}_2$ , and  $\text{NiS}$  again.

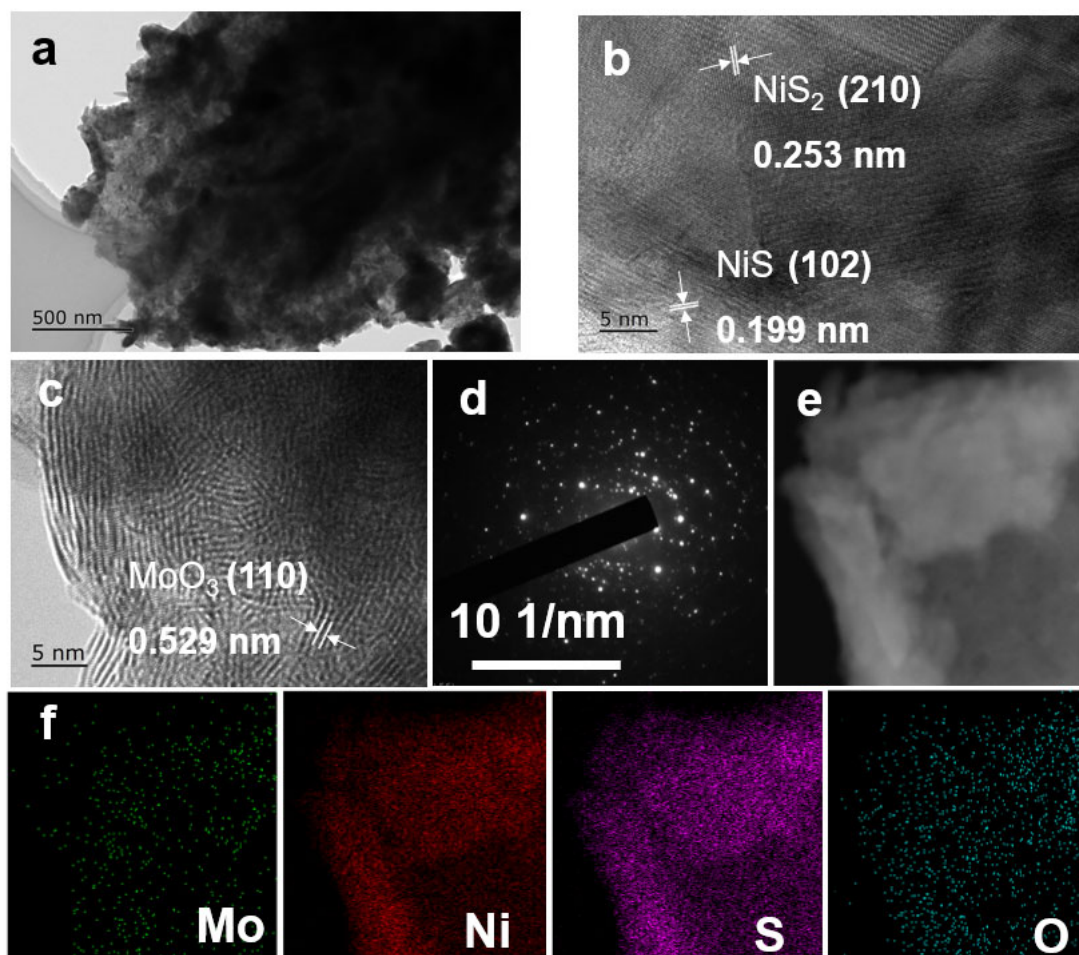


**Figure 4.** (a) TEM images, (b,c) HR-TEM images, (d) SAED pattern, and (e,f) STEM-EDS mapping of 9H5E-CC.

The HER performance of 9H5E-CC was evaluated using a standard three-electrode configuration, with a Pt wire counter electrode and a saturated Ag/AgCl reference electrode in a 1.0 M KOH solution. The electrodeposition time of the Ni layer and the amount of  $(\text{NH}_4)_2\text{MoS}_4$  in the hydrothermal reaction were altered to modulate the quantity of Ni and Mo ingredients in the catalyst, respectively. The catalyst obtained using a too-thick Ni layer was not stable, which was reflected in a large amount of black granules falling off during polarization testing (Figure S3). After determining the ideal experimental parameters, the bare CC, 5E-CC, 9H15E-CC, 9H-CC, and commercial Pt/C catalyst were also tested for further comparison. They were supported on CC with the same method and mass loading. It can be seen that 9H5E-CC, which had excellent HER activity, was second only to the commercial Pt/C and exhibited a better HER activity than the bare CC, 5E-CC, 9H15E-CC, and 9H-CC, as shown in Figure 5a. In detail, only a low overpotential ( $\eta_{10}$ ) of  $-142$  mV could achieve a current density of  $10 \text{ mA cm}^{-2}$ , which is closer to that of the commercial Pt/C than to the bare CC, 5E-CC, 9H15E-CC, and 9H-CC. Compared with the 9H15E-CC sample, which did not contain Mo, the overpotential of 9H5E-CC was very low. There were no particles grown on CC when the hydrothermal reaction was conducted without adding

Ni source (9H-CC), as shown in Figure 1b. Meanwhile, the 5E-CC to 9H15E-CC transition that occurred via a hydrothermal reaction was accompanied by a decay in electrochemical performance. For this phenomenon, we presume that  $\text{MoO}_3$  played a significant role in the catalytic activity, and  $\text{NiS}_x$ , as the cocatalyst, contributed to the formation of the catalyst film.  $\text{MoO}_3$  and  $\text{NiS}_x$  cannot be separated from each other and may be derived from a synergistic effect that improves HER performance.

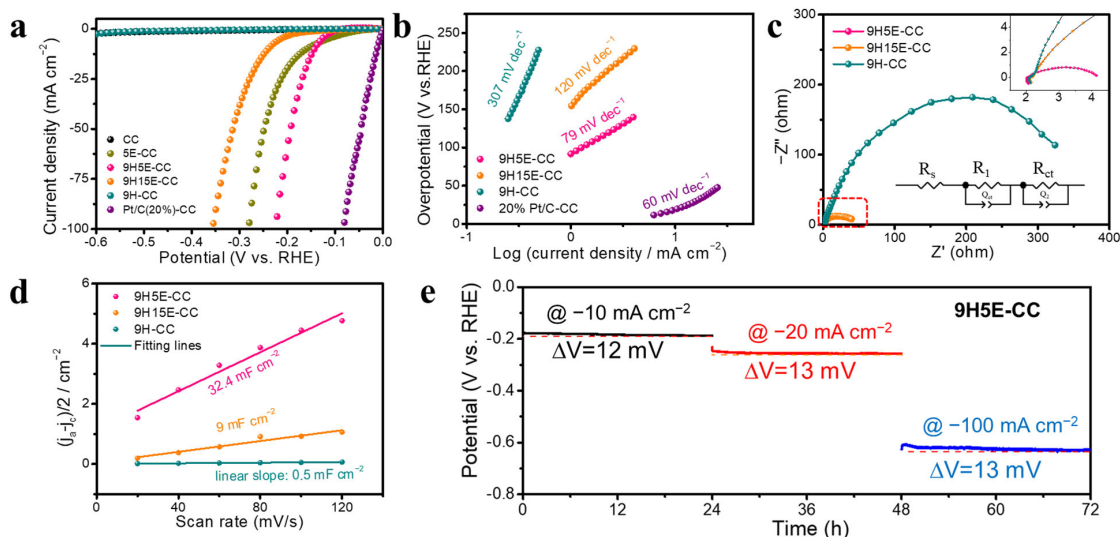


**Figure 5.** Electrocatalytic HER. (a) Polarization curves; (b) Tafel plot; (c) EIS; (d) current density differences ( $\Delta j = j_a - j_c$ ) plotted against scan rate (20, 40, 60, 80, 100, and 120 mV/s); (e) long-term stability measurement of 9H5E-CC sample at  $-10$ ,  $-20$ , and  $-100$  mA  $\text{cm}^{-2}$  for each 24 h.

As shown in Figure 5b, Tafel plots were used to examine the electrocatalysts kinetics of 9H5E-CC. The Tafel slope of 9H5E-CC ( $79$  mV  $\text{dec}^{-1}$ ) is shallower than those of 9H15E-CC ( $120$  mV  $\text{dec}^{-1}$ ) and 9H-CC ( $307$  mV  $\text{dec}^{-1}$ ), and it is close to that of the commercial Pt/C electrocatalyst ( $60$  mV  $\text{dec}^{-1}$ ). This indicates that 9H5E-CC provided a small Tafel slope and fast HER kinetics.  $\text{MoO}_3$  and  $\text{NiS}_x$  composites play an active role in HER kinetics, and the Tafel slope becomes small when the two elements coexist. The electrochemistry kinetics and interfacial properties of catalysts are further shown using Nyquist plots of the EIS measurements in Figure 5c. The Nyquist plots illustrate that the charge transfer resistance ( $R_{ct}$ ) of 9H5E-CC was lower than those of 9H15E-CC and 9H-CC, which indicates the fast charge transfer process and high conductivity of 9H5E-CC (Table S2) [36]. The extremely low  $R_{ct}$  of 9H5E-CC is attributed to the combination of  $\text{MoO}_3$  and  $\text{NiS}_x$  in the film.

To further obtain detailed information on HER performance, the double-layer capacitances ( $C_{dl}$ ) of 9H5E-CC, 9H15E-CC, and 9H-CC were determined using cyclic voltammetry (CV) curves at different scanning rates within a range of potentials (Figure S4). As shown in Figure 5d, the  $C_{dl}$  values of 9H5E-CC, 9H15E-CC, and 9H-CC were determined to be  $32.4$ ,  $9$ , and  $0.5$  mF  $\text{cm}^{-2}$ , respectively [37,38]. This indicates that the presence of Mo has a positive effect on the efficient adsorption and transfer of the reactant. Additionally, long-term stability is a significant standard for evaluating the catalytic performance of HER. Chronoamperometry was performed to evaluate the durability and stability of 9H5E-CC during HER measurement at different constant current densities, as shown in Figure 5e. The 72 h of chronoamperometry consisted of three stages, which are running for 24 h at  $-10$ ,  $-20$ , and  $-100$  mA  $\text{cm}^{-2}$  in turn. This illustrates that 9H5E-CC is highly stable, negligibly changing with potential. During the operational process, the recession in value of potential is 12, 13, and 13 mV at  $-10$ ,  $-20$ , and  $-100$  mA  $\text{cm}^{-2}$ , respectively. According to the analysis of the preceding context, Mo element contributes to catalytic activity while Ni element helps with the film forming. These details prove that the Ni element plays an important role in excellent durability and stability.

9H5E-CC showed weak OER performance and instability, as shown in Figure S3. However, the experimental results show that the catalyst was characterized by great OER performance and stability when the CC substrate was replaced with Co foam (CF) for OER (the method for synthesizing 9H5E-CF was similar to that for 9H5E-CC). Photographic images of the as-obtained samples are shown in Figure S5. As shown in Figure S6a,b, 5E-CF exhibited a dense film structure consisting of fine particles. After the hydrothermal reaction, the Ni particles in 5E-CF transformed into smaller spherical particles that stacked together. Simultaneously, the dense film of 9H5E-CF before polarization acquired a three-dimensional (3D) structure characterized by an increased specific surface area, and its particle sizes reduced after the hydrothermal reaction. This structure facilitated more effective contact between the catalyst and the electrolyte (Figure S6c,d). After electrodeposition and the hydrothermal reaction, a stable and durable catalyst with excellent catalytic performance was obtained via polarization, removing the unnecessary material on the sample's surface. The SEM images of 9H5E-CF before and after polarization are shown in Figures S6c,d and S7a,b. The final sample of 9H5E-CF was examined using electrochemical testing and other measurements. For comparison, bare CF, 5E-CF, 9H15E-CF, 9H-CF, and commercial RuO<sub>2</sub> were also tested, which were supported on CF using the same method or mass loading. The OER performance of 9H5E-CF was also investigated using the standard three-electrode configuration with a Pt-wire counter electrode and a saturated Ag/AgCl reference electrode in 1.0 M KOH solution. As shown in Figure 6a, 9H5E-CF presented high-quality performance. In detail, a relatively low overpotential ( $\eta_{50}$ ) of 294 mV achieved a current density of 50 mA cm<sup>-2</sup>, which is closer to that of commercial RuO<sub>2</sub> than those of the bare CF, 5E-CF, 9H15E-CF, and 9H-CF at low current density. In addition, the catalytic activity of 9H5E-CF was also better than that of the commercial RuO<sub>2</sub> when the potential exceeded 1.58 V vs. RHE. According to the XRD and XPS results, 9H5E-CF contained Mo, Ni, and Co, as shown in Figures S8 and S9.

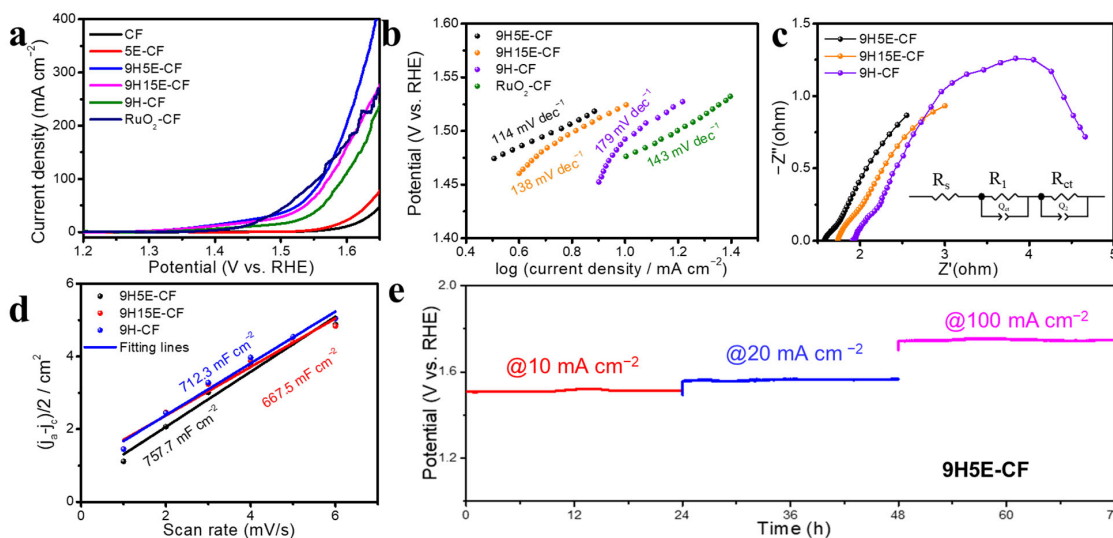


**Figure 6.** Electrocatalytic OER. (a) Polarization curves, (b) Tafel plots, (c) EIS, (d) current density differences ( $\Delta j = j_a - j_c$ ) plotted against different scan rates (1, 2, 3, 4, 5, and 6 mV/s), and (e) long-term stability measurement of 9H5E-CF sample at 10, 20, and 100 mA cm<sup>-2</sup> for each 24 h.

The electrocatalytic kinetics for OER described by the Tafel slopes in Figure 6b. The Tafel slope of the 9H5E-CF sample (114 mV dec<sup>-1</sup>) was smaller than those of 9H15E-CF (138 mV dec<sup>-1</sup>), 9H-CF (179 mV dec<sup>-1</sup>), and commercial RuO<sub>2</sub>-CF electrocatalysts (143 mV dec<sup>-1</sup>). This shows that 9H5E-CF had a small Tafel slope and fast OER kinetics. The Nyquist plots of EIS measurements further show the electrochemistry kinetics and interfacial properties of the catalysts in Figure 6c. The  $R_{ct}$  of 9H5E-CF is illustrated with a Nyquist plot, which is lower than those of 9H15E-CF and 9H-CF, revealing the fast

charge transfer process and high conductivity of 9H5E-CF (Table S3). The extremely low  $R_{ct}$  of 9H5E-CF is due to the combination of  $\text{Co}_2\text{O}_3$ , and  $\text{Mo}_8\text{O}_{23}$  with Ni doping in the films. To further obtain detailed information on OER performance, the ECSAs of 9H5E-CF, 9H15E-CF, and 9H-CF from their  $C_{dl}$  were measured and analyzed using CV curves at different scanning rates, as shown in Figure S10. As shown in Figure 6d, the  $C_{dl}$  values of 9H5E-CF, 9H15E-CF, and 9H-CF are determined to be 757.7, 667.5, and 712.3  $\text{mF cm}^{-2}$ , respectively. This indicates outstanding the efficient adsorption and transfer of the reactant during the OER. The long-term stability of the catalyst is a significant concern for water oxidation. Chronoamperometry was also performed to evaluate the durability and stability of 9H5E-CF during OER measurement at different constant current densities of 10, 20, and 100  $\text{mA cm}^{-2}$ , respectively. Figure 6e illustrates that 9H5E-CF displays excellent stability with a negligible change in potential. As depicted in Figure S7c,d, after the 72 h OER stability test, the bulk structure of 9H5E-CF changed and exhibited a particle-like morphology. However, the structural modification did not have any adverse impact on the catalytic OER performance.

To prove the highly efficient HER and OER activity of 9H5E-CC and 9H5E-CF, a simple two-electrode device was applied for overall water splitting in an alkaline solution. As shown in Figure 7a, the electrolytic cell of 9H5E-CF||9H5E-CC only needed 1.88 V to reach 50  $\text{mA cm}^{-2}$ , which is close to that of commercial  $\text{RuO}_2\text{-CF}||\text{Pt/C}(20\%)\text{-CC}$ . A 1.5 V solar panel was applied as power to drive overall water splitting, as shown in Figure 7b. It is demonstrated that hydrogen and oxygen bubbles continually appeared from the surface of the cathode and anode. The long-term stability of a catalyst is a vital parameter for overall water splitting, so long-term chronoamperometry measurements at 10, 20, and 100  $\text{mA cm}^{-2}$  were obtained to evaluate the durability of 9H5E-CF||9H5E-CC, as shown in Figure 7c. 9H5E-CF||9H5E-CC showed high stability with negligible voltage change. Additionally, compared with the reported bifunctional catalysts for HER, OER, and overall water splitting in alkaline electrolytes, a competitive overpotential of 142 mV ( $\eta_{10}$ ) for HER, 294 mV ( $\eta_{50}$ ) for OER, and 1.88 V (at 50  $\text{mA cm}^{-2}$ ) for overall water splitting were achieved for the  $\text{MoO}_3\text{-NiS}_x$  catalyst, as shown in Table S4 [39–51].

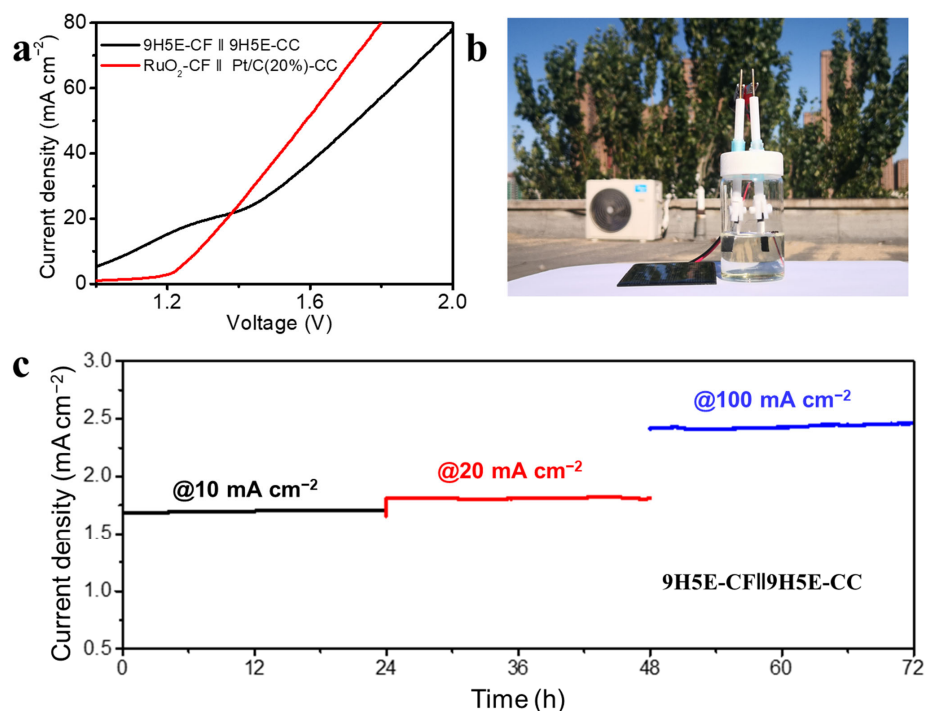


**Figure 7.** Overall water splitting activity of 9H5E-CF||9H5E-CC. (a) Polarization curves, (b) Photographic image of overall water splitting driven by a solar panel, (c) Long-term stability measurement at 10, 20, 100  $\text{mA cm}^{-2}$  for each 24 h.

### 3. Materials and Experiments

#### 3.1. Materials and Chemicals

Nickel sulfate hexahydrate ( $\text{NiSO}_4 \cdot 6\text{H}_2\text{O}$ , 99%), sodium sulfate anhydrous ( $\text{Na}_2\text{SO}_4$ , 99%), thiourea ( $\text{CH}_4\text{N}_2\text{S}$ , 99%), and ammonium tetrathiomolybdate ( $(\text{NH}_4)_2\text{MoS}_4$ , 99.95%) were purchased from Aladdin Reagent Inc, Shanghai, China. Boric acid ( $\text{H}_3\text{BO}_3$ , 99.5%) was purchased from Sinopharm Chemical Reagent Co., Ltd, Shanghai, China. Cobalt foam (CF, areal density  $1400 \text{ g/m}^2$ ) was bought from Alantum Corporation, Seoul, Korea. The carbon cloth (CC, thickness: 0.33 mm, W0S1009, CeTech Co., Ltd, Taiwan, China) was cut into  $1 \text{ cm} \times 2.5 \text{ cm}$  sheets and treated in a round-bottomed flask fitted with a reflux condenser to mix the solution, which contained nitric acid (7.5 wt%) and sulfuric acid (2.5 wt%), at  $80 \text{ }^\circ\text{C}$  for 3 h. Then, it was cleaned with ethanol and DI water for 10 min, respectively, followed by drying at  $60 \text{ }^\circ\text{C}$  for 4 h.

#### 3.2. Electrodeposition of Ni Film on CC

5E-CC was fabricated using a typical two-electrode device with a Rigol-DP832A (RIGOL Technologies, Co. Ltd, Beijing, China) workstation. The deposition bath contained 0.05 M  $\text{Na}_2\text{SO}_4$ , 0.5 M  $\text{H}_3\text{BO}_3$ , and 0.1 M  $\text{NiSO}_4$ . While electrodepositing, the treated CC acted as the cathode; Pt wire was used as the anode electrode. 5E-CC was electrodeposited with a geometric area of  $1.0 \text{ cm}^2$ . The depositing was performed at room temperature with a constant current of  $-100 \text{ mA}$  for 5 min. After electrolysis, the as-prepared catalysts were washed using deionized water and ethanol and dried under airflow.

#### 3.3. Preparation of 9H5E-CC and 9H5E-CF

The 9H5E-CC catalyst was synthesized via a hydrothermal reaction of  $\text{CH}_4\text{N}_2\text{S}$ ,  $(\text{NH}_4)_2\text{MoS}_4$ , and 5E-CC in  $\text{H}_2\text{O}$ . Typically, 0.01 M  $(\text{NH}_4)_2\text{MoS}_4$  and 0.5 M  $\text{CH}_4\text{N}_2\text{S}$  were dissolved in 50 mL of DI water, and the mixed solution was stirred at room temperature for 30 min. Then, the 5E-CC and mixed solution were transferred into a 100 mL Teflon-lined stainless-steel autoclave and maintained at  $180 \text{ }^\circ\text{C}$  for 9 h. Afterward, the autoclave was cooled to room temperature naturally; the carbon cloth was taken out and washed with DI water and ethanol. The washed sample was dried via airflow. For comparison, the control sample was synthesized following the same chemical method as used for 9H15E-CC, 9H-CC, and 9H25E-CC without adding  $(\text{NH}_4)_2\text{MoS}_4$  or electrodepositing Ni or thiourea, respectively. We conducted a hydrothermal reaction using CC merely with thiourea or  $(\text{NH}_4)_2\text{MoS}_4$  for 9H1-CC or 9H2-CC, respectively.

Furthermore, we replaced carbon cloth with Co foam mainly for the OER process; the remainder of the synthesis method was similar to that described above, except polarization for 1 h in  $10 \text{ mA cm}^{-2}$  was the last step. The obtained samples were denoted as CF, 5E-CF, 9H5E-CF, 9H1-CF, 9H15E-CF, 9H-CF, 9H25E-CF, and 9H2-CF, respectively. The detailed experimental parameters for the samples are shown in Table S1. After the reaction, the weights of 9H5E-CC and 9H5E-CF increased by 6.03 mg and 2.8 mg, respectively.

#### 3.4. Preparation of Pt/C(20%)-CC and $\text{RuO}_2$ -CF

For comparison, the typical noble metal catalysts of Pt/C(20%) and  $\text{RuO}_2$  were fabricated on carbon cloth and Co foam for HER and OER, respectively. The ink was prepared by dispersing 6.03 mg of Pt/C(20%) catalyst (or 2.8 mg of  $\text{RuO}_2$ ) in 0.8 mL of deionized water, 0.8 mL of isopropanol, and 14  $\mu\text{L}$  of Nafion. The resultant mixed solution was then sonicated for 30 min to generate a uniform catalyst ink. Finally, all of the ink was dropped directly onto the surface of carbon cloth (or Co foam) over an area of  $1 \times 1 \text{ cm}^2$  and dried at  $95 \text{ }^\circ\text{C}$  for 12 h.

#### 3.5. Electrochemical Characterization

Electrochemical characterizations were conducted using a CHI660E electrochemical analyzer (CH Instruments, Inc., Shanghai, China) at room temperature. Hydrogen and oxygen evolution measurements were recorded in 1 M KOH using the standard three-

electrode system with Ag/AgCl (in 3 M KCl solution) as the reference electrode and a Pt wire as the counter electrode. The HER and OER potentials versus Ag/AgCl were converted to RHE with the help of the following equation:

$$E_{\text{RHE}} = E_{\text{Ag/AgCl}} + 0.059 \times \text{pH} + 0.197$$

Before OER testing, for the electrode synthesized from Co foam, we performed an approximately two-hour chronopotentiometry procedure at  $10 \text{ mA cm}^{-2}$  to remove the redundant components and achieve stabilization.

### 3.6. Material Characterization

The crystallinity and crystal structure of the samples were characterized using Bruker D8 Advance X-ray diffraction (XRD, Karlsruhe, Germany) with a Cu K $\alpha$  source. The morphologies of the samples and elementary composition were determined using a scanning electron microscope (SEM, ZEISS Sigma 300, Jena, Germany) with energy-dispersive spectroscopy (EDS, Oxford Instruments, INCA x-sight, Oxford, UK). A transmission electron microscope (TEM, JEOL JEM-2100F operating at 100 kV, Japan) was applied to meticulously characterize the crystal structure. X-ray photoelectron spectroscopy (XPS, Thermo ESCALAB 250XI, Carlsbad, CA, USA) was conducted with Al K $\alpha$  radiation.

## 4. Conclusions

In summary, 9H5E-CC and 9H5E-CF were synthesized for HER and OER using a facile method. 9H5E-CF || 9H5E-CC achieved 1.88 V at  $50 \text{ mA cm}^{-2}$  for full water splitting. Highly stable 9H5E-CC electrodes were synthesized via electrodeposition and hydrothermal reactions, which produced a stable film on the CC via the dissolution of a galvanized Ni coating and a MoO<sub>3</sub>-NiS<sub>x</sub> film of 9H5E-CC catalysts. A highly active 9H5E-CF electrode was also fabricated via electrodeposition and hydrothermal reactions; we obtained a stable and durable catalyst with excellent OER performance via anodizing to remove unnecessary material from the sample surface. This electrochemical performance, which is close to that of commercial Pt and RuO<sub>2</sub>, enables the development of an industrialized water splitting system for energy conversion. Our study offers a method for developing highly active and more electrochemically stable electrodes for water splitting.

**Supplementary Materials:** The following supporting information can be downloaded at: <https://www.mdpi.com/article/10.3390/catal13111426/s1>, Figure S1: EDS spectrum of intermediate products of 1H5E-CC; Figure S2: XRD patterns of 5E-CC and CC; Figure S3: Polarization curve of 9H5E-CC for OER; Figure S4: CV curves showing the capacitive performance C<sub>dl</sub> of 9H5E-CC, 9H-CC, and 9H15E-CC. Figure S5: Photographic images of the as-prepared samples on CF; Figure S6: SEM images of 5E-CF and 9H5E-CF before polarization; Figure S7: SEM images of 9H5E-CF before and after running chronopotentiometry; Figure S8: XRD of 9H5E-CF before 2 h chronopotentiometry procedure; Figure S9: XPS spectra of 9H5E-CF. Figure S10: CV curves showing the capacitive performance C<sub>dl</sub> of 9H5E-CF, 9H-CF, and 9H15E-CF. Table S1: Listing of the experimental parameters for fabricating the samples; Table S2: R<sub>s</sub> and R<sub>ct</sub> values of 9H5E-CC, 9H-CC, and 9H15-CC; Table S3: R<sub>s</sub> and R<sub>ct</sub> values of 9H5E-CF, 9H-CF, and 9H15-CF; Table S4: Comparison of the water splitting performance of the catalyst in this study with that of other reported bifunctional catalysts in 1 M KOH. References [39–51] are cited in the Supplementary Materials.

**Author Contributions:** Conceptualization, S.Z. and J.Y.Z.; methodology, S.Z. and T.L.; software, S.Z.; validation, T.L.; formal analysis, S.Z. and S.Y.; investigation, S.Z.; resources, S.Z. and J.Y.Z.; data curation, S.Z., H.Y. and Q.S.; writing—original draft preparation, S.Z.; writing—review and editing, S.Z., T.L. and J.Y.Z.; visualization, S.Z.; supervision, J.Y.Z.; project administration, J.Y.Z. All authors have read and agreed to the published version of the manuscript.

**Funding:** This work was supported by the National Natural Science Foundation of China (grant no. 51902292).

**Data Availability Statement:** The data presented in this study are available upon request from the corresponding author.

**Acknowledgments:** The authors gratefully thank the Modern Analysis and Gene Sequencing Center of Zhengzhou University for the XRD test.

**Conflicts of Interest:** The authors declare no conflict of interest.

## References

1. Karmakar, A.; Karthick, K.; Sankar, S.S.; Kumaravel, S.; Madhu, R.; Kundu, S. A Vast Exploration of Improvising Synthetic Strategies for Enhancing the OER Kinetics of LDH Structures: A Review. *J. Mater. Chem. A* **2021**, *9*, 1314–1352. [[CrossRef](#)]
2. Lv, Z.; Mahmood, N.; Tahir, M.; Pan, L.; Zhang, X.; Zou, J.J. Fabrication of Zero to Three Dimensional Nanostructured Molybdenum Sulfides and Their Electrochemical and Photocatalytic Applications. *Nanoscale* **2016**, *8*, 18250–18269. [[CrossRef](#)] [[PubMed](#)]
3. Mansingh, S.; Das, K.K.; Parida, K. HERs in an Acidic Medium over MoS<sub>2</sub> nanosheets: From Fundamentals to Synthesis and the Recent Progress. *Sustain. Energy Fuels* **2021**, *5*, 1952–1987. [[CrossRef](#)]
4. Xiao, X.; Tao, L.; Li, M.; Lv, X.; Huang, D.; Jiang, X.; Pan, H.; Wang, M.; Shen, Y. Electronic Modulation of Transition Metal Phosphide: Via Doping as Efficient and PH-Universal Electrocatalysts for Hydrogen Evolution Reaction. *Chem. Sci.* **2018**, *9*, 1970–1975. [[CrossRef](#)] [[PubMed](#)]
5. Li, S.H.; Qi, M.Y.; Tang, Z.R.; Xu, Y.J. Nanostructured Metal Phosphides: From Controllable Synthesis to Sustainable Catalysis. *Chem. Soc. Rev.* **2021**, *50*, 7539–7586. [[CrossRef](#)] [[PubMed](#)]
6. Chen, H.; Gao, Y.; Ye, L.; Yao, Y.; Chen, X.; Wei, Y.; Sun, L. A Cu<sub>2</sub>Se-Cu<sub>2</sub>O Film Electrodeposited on Titanium Foil as a Highly Active and Stable Electrocatalyst for the Oxygen Evolution Reaction. *Chem. Commun.* **2018**, *54*, 4979–4982. [[CrossRef](#)] [[PubMed](#)]
7. Yao, D.; Gu, L.; Zuo, B.; Weng, S.; Deng, S.; Hao, W. A Strategy for Preparing High-Efficiency and Economical Catalytic Electrodes toward Overall Water Splitting. *Nanoscale* **2021**, *13*, 10624–10648. [[CrossRef](#)]
8. Zhai, W.; Sakthivel, T.; Chen, F.; Du, C.; Yu, H.; Dai, Z. Amorphous Materials for Elementary-Gas-Involved Electrocatalysis: An Overview. *Nanoscale* **2021**, *13*, 19783–19811. [[CrossRef](#)]
9. Li, B.; Wang, K.; Ren, J.; Qu, P. NiOOH@Cobalt Copper Carbonate Hydroxide Nanorods as Bifunctional Electrocatalysts for Highly Efficient Water and Hydrazine Oxidation. *New J. Chem.* **2022**, *46*, 7615–7625. [[CrossRef](#)]
10. Shao, M.; Chen, H.; Cao, Y.; Fu, S.; Hao, S.; Chen, M.; Jin, J.; Wang, W.; Wu, Y.; Cui, L. Phase Transition in V-doped Cobalt Hydroxide for a Superior Alkaline Hydrogen Evolution Reaction. *Chem. Commun.* **2022**, *58*, 12859–12862. [[CrossRef](#)]
11. Jung, H.; Choung, S.; Han, J.W. Design Principles of Noble Metal-free Electrocatalysts for Hydrogen Production in Alkaline Media: Combining Theory and Experiment. *Nanoscale Adv.* **2021**, *3*, 6797–6826. [[CrossRef](#)] [[PubMed](#)]
12. Yan, L.; Ren, Y.; Zhang, X.; Sun, Y.; Ning, J.; Zhong, Y.; Teng, B.; Hu, Y. Electronic Modulation of Composite Electrocatalysts Derived from Layered NiFeMn Triple Hydroxide Nanosheets for Boosted Overall Water Splitting. *Nanoscale* **2019**, *11*, 20797–20808. [[CrossRef](#)] [[PubMed](#)]
13. Li, B.; Li, J.; Liu, X.; Guo, J.; Sun, Y.; Zhang, X. Se-Doped CoP Nanoneedle Arrays Grown on Carbon Cloth for an Efficient Hydrogen Evolution Reaction. *Energy Fuels* **2022**, *36*, 13212–13217. [[CrossRef](#)]
14. Liu, Y.; Tian, Z.; Xu, Q.; Yang, Y.; Zheng, Y.; Pan, H.; Chen, J.; Wang, Z.; Zheng, W. Controllable Synthesis of a Loofah-Like Cobalt-Nickel Selenide Network as an Efficient Electrocatalyst for the Hydrogen Evolution Reaction. *ACS Appl. Mater. Interfaces* **2022**, *14*, 8963–8973. [[CrossRef](#)] [[PubMed](#)]
15. Murthy, R.; Neelakantan, S.C. Graphitic Carbon Cloth-Based Hybrid Molecular Catalyst: A Non-Conventional, Synthetic Strategy of the Drop Casting Method for a Stable and Bifunctional Electrocatalyst for Enhanced Hydrogen and Oxygen Evolution Reactions. *ACS Omega* **2022**, *7*, 32604–32614. [[CrossRef](#)] [[PubMed](#)]
16. Gudal, C.C.; Pan, U.N.; Paudel, D.R.; Kandel, M.R.; Kim, N.H.; Lee, J.H. Bifunctional P-Intercalated and Doped Metallic (1T)-Copper Molybdenum Sulfide Ultrathin 2D-Nanosheets with Enlarged Interlayers for Efficient Overall Water Splitting. *ACS Appl. Mater. Interfaces* **2022**, *14*, 14492–14503. [[CrossRef](#)] [[PubMed](#)]
17. Yuan, W.; Li, Y.; Liang, L.; Wang, F.; Liu, H. Dual-Anion Doping Enables NiSe<sub>2</sub> Electrocatalysts to Accelerate Alkaline Hydrogen Evolution Reaction. *ACS Appl. Energy Mater.* **2022**, *5*, 5036–5043. [[CrossRef](#)]
18. Chen, Y.; Wang, D.; Meng, T.; Xing, Z.; Yang, X. Modulating the Electronic Structure by Ruthenium Doping Endows Cobalt Phosphide Nanowires with Enhanced Alkaline Hydrogen Evolution Activity. *ACS Appl. Energy Mater.* **2022**, *5*, 697–704. [[CrossRef](#)]
19. Alsabban, M.M.; Eswaran, M.K.; Peramaiah, K.; Wahyudi, W.; Yang, X.; Ramalingam, V.; Hedhili, M.N.; Miao, X.; Schwingenschlögl, U.; Li, L.J.; et al. Unusual Activity of Rationally Designed Cobalt Phosphide/Oxide Heterostructure Composite for Hydrogen Production in Alkaline Medium. *ACS Nano* **2022**, *16*, 3906–3916. [[CrossRef](#)]
20. Dong, Y.; Fang, Z.; Yang, W.; Tang, B.; Liu, Q. Integrated Bifunctional Electrodes Based on Amorphous Co-Ni-S Nanoflake Arrays with Atomic Dispersity of Active Sites for Overall Water Splitting. *ACS Appl. Mater. Interfaces* **2022**, *14*, 10277–10287. [[CrossRef](#)]
21. Zhang, K.; Jiang, P.; Gu, Q.; Leng, Y.; Zhang, P. Design of a High-Efficiency Bifunctional Electrocatalyst: Rich-Nitrogen-Doped Reduced Graphene Oxide-Modified Carbon Cloth-Growing Nickel-Iron Complex Oxides for Overall Water Splitting. *Energy and Fuels* **2022**, *36*, 4911–4923. [[CrossRef](#)]
22. Deng, K.; Liu, P.; Liu, X.; Zheng, J.; Zhao, R.; Li, H.; Tian, W.; Ji, J. Synergistic Coupling of SnS<sub>2</sub> Nanosheet Arrays with Ni/Fe Dual Metal and Ru Nanodots via a Cation Exchange Strategy for Overall Water Splitting. *Ind. Eng. Chem. Res.* **2022**, *61*, 382–391. [[CrossRef](#)]

23. Lin, W.; Zhang, B.; Jiang, J.; Liu, E.; Sha, J.; Ma, L. Anionic and Cationic Co-Substitutions of S into Vertically Aligned WTe<sub>2</sub> Nanosheets as Catalysis for Hydrogen Evolution under Alkaline Conditions. *ACS Appl. Nano Mater.* **2022**, *5*, 7123–7131. [[CrossRef](#)]
24. Zheng, Y.; Xu, J.; Zhu, Y.; Zhang, T.; Yang, D.; Qiu, F. Hierarchical Coralline-like (NiCo)S<sub>2</sub>@MoS<sub>2</sub> Nanowire Arrays to Accelerate H<sub>2</sub> Release for an Efficient Hydrogen Evolution Reaction. *Inorg. Chem.* **2022**, *61*, 5352–5362. [[CrossRef](#)] [[PubMed](#)]
25. You, M.; Du, X.; Hou, X.; Wang, Z.; Zhou, Y.; Ji, H.; Zhang, L.; Zhang, Z.; Yi, S.; Chen, D. In-Situ Growth of Ruthenium-Based Nanostructure on Carbon Cloth for Superior Electrocatalytic Activity towards HER and OER. *Appl. Catal. B Environ.* **2022**, *317*, 121729. [[CrossRef](#)]
26. Huang, G.; Zhao, L.; Yuan, S.; Li, N.; Jing, S. Iron Doped Mesoporous Cobalt Phosphide with Optimized Electronic Structure for Enhanced Hydrogen Evolution. *Int. J. Hydrog. Energy* **2022**, *47*, 14767–14776. [[CrossRef](#)]
27. Gu, C.; Zhou, G.; Yang, J.; Pang, H.; Zhang, M.; Zhao, Q.; Gu, X.; Tian, S.; Zhang, J.; Xu, L.; et al. NiS/MoS<sub>2</sub> Mott-Schottky Heterojunction-Induced Local Charge Redistribution for High-Efficiency Urea-Assisted Energy-Saving Hydrogen Production. *Chem. Eng. J.* **2022**, *443*, 136321. [[CrossRef](#)]
28. Yao, N.; Li, P.; Zhou, Z.; Zhao, Y.; Cheng, G.; Chen, S.; Luo, W. Synergistically Tuning Water and Hydrogen Binding Abilities Over Co<sub>4</sub>N by Cr Doping for Exceptional Alkaline Hydrogen Evolution Electrocatalysis. *Adv. Energy Mater.* **2019**, *9*, 1902449. [[CrossRef](#)]
29. Chen, B.; Kim, D.; Zhang, Z.; Lee, M.; Yong, K. MOF-Derived NiCoZnP Nanoclusters Anchored on Hierarchical N-Doped Carbon Nanosheets Array as Bifunctional Electrocatalysts for Overall Water Splitting. *Chem. Eng. J.* **2021**, *422*, 130533. [[CrossRef](#)]
30. Tang, W.J.; Wang, X.L.; Xie, D.; Xia, X.H.; Gu, C.D.; Tu, J.P. Hollow Metallic 1T MoS<sub>2</sub> Arrays Grown on Carbon Cloth: A Freestanding Electrode for Sodium Ion Batteries. *J. Mater. Chem. A* **2018**, *6*, 18318–18324. [[CrossRef](#)]
31. Li, W.; Zhang, Z.; Zhang, W.; Zou, S. MoS<sub>2</sub> Nanosheets Supported on Hollow Carbon Spheres as Efficient Catalysts for Electrochemical Hydrogen Evolution Reaction. *ACS Omega* **2017**, *2*, 5087–5094. [[CrossRef](#)] [[PubMed](#)]
32. Zeng, J.R.; Gao, M.Y.; Zhang, Q.B.; Yang, C.; Li, X.T.; Yang, W.Q.; Hua, Y.X.; Xu, C.Y.; Li, Y. Facile Electrodeposition of Cauliflower-like S-Doped Nickel Microsphere Films as Highly Active Catalysts for Electrochemical Hydrogen Evolution. *J. Mater. Chem. A* **2017**, *5*, 15056–15064. [[CrossRef](#)]
33. Niu, Y.; Qian, X.; Zhuang, J.; Liu, H.; Hou, L. MoS<sub>2</sub>/Ni-CoS<sub>x</sub> Porous Nanocubes Derived from Ni-Co Prussian-Blue Analogs as Enhanced Pt-Free Electrode Catalysts for High-Efficiency Dye-Sensitized Solar Cells. *J. Power Sources* **2019**, *440*, 227121. [[CrossRef](#)]
34. Che, Q.; Li, Q.; Chen, X.; Tan, Y.; Xu, X. Assembling Amorphous (Fe-Ni)Co<sub>x</sub>-OH/Ni<sub>3</sub>S<sub>2</sub> Nanohybrids with S-Vacancy and Interfacial Effects as an Ultra-Highly Efficient Electrocatalyst: Inner Investigation of Mechanism for Alkaline Water-to-Hydrogen/Oxygen Conversion. *Appl. Catal. B Environ.* **2020**, *263*, 118338. [[CrossRef](#)]
35. Gu, W.; Yan, Y.; Zhang, C.; Ding, C.; Xian, Y. One-Step Synthesis of Water-Soluble MoS<sub>2</sub> Quantum Dots via a Hydrothermal Method as a Fluorescent Probe for Hyaluronidase Detection. *ACS Appl. Mater. Interfaces* **2016**, *8*, 11272–11279. [[CrossRef](#)] [[PubMed](#)]
36. Shi, H.; Sun, X.Y.; Liu, Y.; Zeng, S.P.; Zhang, Q.H.; Gu, L.; Wang, T.H.; Han, G.F.; Wen, Z.; Fang, Q.R.; et al. Multicomponent Intermetallic Nanoparticles on Hierarchical Metal Network as Versatile Electrocatalysts for Highly Efficient Water Splitting. *Adv. Funct. Mater.* **2023**, *33*, 2214412. [[CrossRef](#)]
37. Kwon, J.; Sun, S.; Choi, S.; Lee, K.; Jo, S.; Park, K.; Kim, Y.K.; Park, H.B.; Park, H.Y.; Jang, J.H.; et al. Tailored Electronic Structure of Ir in High Entropy Alloy for Highly Active and Durable Bifunctional Electrocatalyst for Water Splitting under an Acidic Environment. *Adv. Mater.* **2023**, *35*, 2300091. [[CrossRef](#)]
38. Liu, D.; Wu, Z.; Liu, J.; Gu, H.; Li, Y.; Li, X.; Liu, S.; Liu, S.; Zhang, J. Heteroatom Doped Amorphous/Crystalline Ruthenium Oxide Nanocages as a Remarkable Bifunctional Electrocatalyst for Overall Water Splitting. *Small* **2023**, *19*, 2207235. [[CrossRef](#)]
39. Pei, Z.; Qin, T.; Tian, R.; Ou, Y.; Guo, X. Construction of an Amethyst-like MoS<sub>2</sub>@Ni<sub>9</sub>S<sub>8</sub>/Co<sub>3</sub>S<sub>4</sub> Rod Electrocatalyst for Overall Water Splitting. *Nanomaterials* **2023**, *13*, 2302. [[CrossRef](#)]
40. Qian, Y.; Yu, J.; Zhang, F.; Fei, Z.; Shi, H.; Kang, D.J.; Pang, H. Hierarchical Binary Metal Sulfides Nanoflakes Decorated on Graphene with Precious-Metal-like Activity for Water Electrolysis. *Chem. Eng. J.* **2023**, *470*, 144372. [[CrossRef](#)]
41. Feng, L.; Zhou, J.; Xiao, J.; Chen, F.; Zhao, Z.; Liu, M.; Zhang, N.; Gao, F. Simple Cathodic Deposition of FeS/NiS-Activated Ni/NiO Heterojunctions for High-Concentration Overall Water Splitting Reactions. *Int. J. Hydrog. Energy* **2023**, *48*, 29852–29864. [[CrossRef](#)]
42. Wan, Z.; Zhang, Y.; Ren, Q.; Li, X.; Yu, H.; Zhou, W.; Ma, X.; Xuan, C. Interface Engineering of NiS/NiCo<sub>2</sub>S<sub>4</sub> Heterostructure with Charge Redistribution for Boosting Overall Water Splitting. *J. Colloid Interface Sci.* **2024**, *653*, 795–806. [[CrossRef](#)] [[PubMed](#)]
43. Liu, Z.; Jia, H.; Wang, H.; Wang, Y.; Zhang, G. Constructing S-Deficient Nickel Sulfide/N-Doped Carbon Interface for Improved Water Splitting Activity. *Nanoscale* **2023**, *15*, 16039–16048. [[CrossRef](#)] [[PubMed](#)]
44. Kim, K.H.; Hong, D.; Kim, M.G.; Choi, W.; Min, T.; Kim, Y.M.; Choi, Y.H. Improving Electrocatalytic Activity of MoO<sub>3</sub> for the Oxygen Evolution Reaction by Incorporation of Li Ions. *ACS Mater. Lett.* **2023**, *5*, 1196–1201. [[CrossRef](#)]
45. Yang, M.; Shi, B.; Tang, Y.; Lu, H.; Wang, G.; Zhang, S.; Sarwar, M.T.; Tang, A.; Fu, L.; Wu, M.; et al. Interfacial Chemical Bond Modulation of Co<sub>3</sub>(PO<sub>4</sub>)<sub>2</sub>-MoO<sub>3-x</sub> Heterostructures for Alkaline Water/Seawater Splitting. *Inorg. Chem.* **2023**, *62*, 2838–2847. [[CrossRef](#)] [[PubMed](#)]
46. Guo, F.; Li, W.; Liu, Y.; Chen, Q.; Zhong, Q. Heterogeneous Fe-Doped NiCoP-MoO<sub>3</sub> Efficient Electrocatalysts for Overall Water Splitting. *Langmuir* **2023**, *39*, 1042–1050. [[CrossRef](#)] [[PubMed](#)]
47. Yu, N.; Ke, H.; Yu, H.; Wu, X.; Li, S.; Chen, G.; Wang, J.; Cai, N.; Xue, Y.; Yu, F. Polysulfide-Induced Synthesis of Coral-Like MoS<sub>2</sub>/NiS<sub>2</sub> Nanostructures for Overall Water Splitting. *ACS Appl. Nano Mater.* **2023**, *6*, 5136–5144. [[CrossRef](#)]
48. Yu, X.; Mei, J.; Du, Y.; Cheng, X.; Wang, X.; Wu, Q. Engineered Interface of Three-Dimensional Coralliform NiS/FeS<sub>2</sub> Heterostructures for Robust Electrocatalytic Water Cleavage. *Nano Res.* **2023**, *5*, 740–749. [[CrossRef](#)]

49. Prakash, C.; Sahoo, P.; Yadav, R.; Pandey, A.; Singh, V.K.; Dixit, A. Nanoengineered Zn-Modified Nickel Sulfide (NiS) as a Bifunctional Electrocatalyst for Overall Water Splitting. *Int. J. Hydrog. Energy* **2023**, *48*, 21969–21980. [[CrossRef](#)]
50. Wang, Q.; Du, X.; Zhang, X. Construction of CoS/NiS@CuS with Dandelion Flower-like Heterostructures as Efficient Catalysts for Overall Urea Splitting. *Int. J. Hydrog. Energy* **2023**, *48*, 24342–24355. [[CrossRef](#)]
51. Tong, X.; Liao, W.; Zhai, Y.; Liu, P.; Yang, Q.; Chen, T. NiO/Co<sub>2</sub>P Nanosheets with Heterogeneous Structure as a Multifunctional Catalyst for Overall Water Splitting. *J. Electrochem. Soc.* **2023**, *170*, 063509. [[CrossRef](#)]

**Disclaimer/Publisher's Note:** The statements, opinions and data contained in all publications are solely those of the individual author(s) and contributor(s) and not of MDPI and/or the editor(s). MDPI and/or the editor(s) disclaim responsibility for any injury to people or property resulting from any ideas, methods, instructions or products referred to in the content.